Insight into the praseodymium effect on the NH3-SCR reaction pathways over W or Nb supported ceria-zirconia based catalysts

Charlotte Croisé, Rémy Pointecouteau, Joudia Akil, Alain Demourgues, Nicolas Bion, Xavier Courtois, Fabien Can

Insight into the praseodymium effect on the NH_3-SCR reaction pathways over W or Nb supported ceria-zirconia based catalysts

Charlotte Croisé[a], Rémy Pointecouteau[ab], Joudia Akil[a], Alain Demourgues[b], Nicolas Bion[a], Xavier Courtois[a], Fabien Can[a]

[a] *Institut de Chimie des Milieux et Matériaux de Poitiers (IC2MP), Université de Poitiers, CNRS, UMR 7285, 4 Rue Michel Brunet, TSA 51106, F-86073 Poitiers 9, France*
[b] *Institut de Chimie de la Matière Condensée de Bordeaux (ICMCB), Université de Bordeaux, Bordeaux INP, CNRS, UMR 5026, 87 Avenue du Dr Albert Schweitzer, 33600 Pessac, France*

Abstract

The partial substitution of zirconium for praseodymium in a ceria-zirconia support was studied for WO_3 or Nb_2O_5 supported catalysts dedicated to the NO_x SCR by NH_3. This partial substitution favored the support reducibility, but both niobium and tungsten impregnation strongly inhibited the redox behaviors of the support. Concomitantly, Nb_2O_5 and WO_3 also provided acidic sites but praseodymium noticeably inhibited the ammonia storage, especially for WO_3-containing sample. Finally, praseodymium drastically decreased the deNO_x performances. Additional NO and NH_3 oxidation experiments were performed and the various redox and acidic behaviors of all the studied materials were suitable to provide an overview of the reactional pathways which begins by the oxidative dehydrogenation of NH_3 on acid sites. The generated species react either with oxygen species or with gaseous NO, reflecting a strong competition between the NO_x SCR and NH_3 oxidation together with the formation of a key intermediate in the nitrogen oxides reduction.

1. Introduction

The NO_x selective catalytic reduction (SCR) by NH_3 is used worldwide to reach the stricter emission standards for mobile and stationary sources. The two main considered reactions respect the "standard SCR" (Eq. 1) and the "fast SCR" (Eq. 2) stoichiometry, depending on the involvement of NO_2.

$$2NH_3 + 2NO + ½O_2 \rightarrow 2N_2 + 3H_2O \quad (1)$$

$$2NH_3 + NO + NO_2 \rightarrow 2N_2 + 3H_2O \quad (2)$$

Actually, the activity obtained in standard SCR condition is largely improved by favoring the oxidation of NO to NO_2 in order to achieve an optimal NO_2/NO_x ratio of 0.5 corresponding to the "fast SCR" stoichiometry. Initially developed in the 1970s for stationary sources using V_2O_5-WO_3-TiO_2 catalysts [1], the NH_3-SCR technology was adapted to heavy-duty vehicles in the 2000s. Ammonia is then obtained by decomposition of an aqueous solution of urea (Adblue®) injected in the exhaust pipe [2,3]. However, the current Euro 6/VI standards for vehicles impose the presence of a diesel particulate filter (DPF) to treat the soot. Unfortunately, vanadia-containing catalysts are not compatible with exotherms generated by the DPF regenerations (combustion of the stored soot) due to the possible V_2O_5 sublimation [4]. Zeolite-based catalysts exchanged with copper or iron were then developed, with suitable structures exhibiting small pores (chabazite, ferrierite,…) for thermal stability [5]. However, some drawbacks remain: zeolite-based catalysts are highly sensitive to the NO_2/NO_x inlet ratio and undesired N_2O (powerful greenhouse effect gas) can be emitted. Various vanadium free oxide based catalysts such as $Fe_2O_3/WO_3/ZrO_2$ [6], MnO_x–CeO_2 [7] or Nb-MnO_x [8] have therefore been proposed to overcome the drawbacks of metal-exchanged zeolites. Besides, to obtain suitable thermal stability for automotive application, zirconia or ceria-zirconia based support (CeZr) were proposed [9,10].

SCR oxide catalysts should exhibit both redox and acidic properties but the deNO_x mechanism over vanadium free catalysts is still subject to discussion. Acidic properties are claimed to ensure the adsorption of ammonia on Lewis or Brønsted acid sites. Ammonia adsorption is argued to be the first step of the complex NO_x removal mechanism and results in hydrogen abstraction to provide —NH_2 amide type species. Hydrogen migration is involved in both (i) acidity conversion from Lewis to Brønsted acid sites transformation at T > 300 °C and (ii) support re-oxidation with O_2 for the

redox loop of the deNO$_x$ reaction [11]. Moreover, redox behaviors are necessary to ensure the SCR reaction by oxidizing the NH$_2$ species together with catalyst reduction (typically cerium reduction for the samples studied in this work). Consequently, oxygen activation by storage/release properties is beneficial to SCR performances. Overall, reaction mechanism involves two independent cycles, with (i) acid cycle route for NH$_3$ adsorption and (ii) redox pathway for NH$_x$-like species activation [12]. Additionally, redox behaviors also potentially promote the NO to NO$_2$ oxidation reaction, allowing a better SCR efficiency and a lower sensitivity to the DOC performance (Diesel Oxidation Catalyst placed upstream). Moreover, the usual standard and fast NH$_3$ SCR stoichiometry (Eqs. 1 and 2) respect a NO$_x$: NH$_3$ ratio of 1 : 1. It induces that the consumption of NH$_3$ by O$_2$ must be prohibited to avoid a lack in reductant availability or an over-injection of reductant. To get a global overview of the deNO$_x$ process, including the reaction intermediates involved in the NH$_3$-NO$_x$ and NH$_3$-O$_2$ competition reactions, catalysts with distinct intrinsic properties resulting in various catalytic performance are required.

Ceria-zirconia based supports appear adequate for the intended application because the redox behaviors (oxygen availability and mobility) could be improved by introducing other rare earth elements. With this aim, praseodymium was selected because of its mixed valences between Pr^{IV} and Pr^{III} [13,14]. Insertion of praseodymium was also reported to improve the thermal stability of ceria-zirconia mixed oxides [15,16]. In fact, a Zr-rich composition ($Ce_{0,2}Zr_{0,8}O_2$) was selected as reference support together with a partial substitution of zirconium by praseodymium ($Ce_{0,2}Zr_{0,6}Pr_{0,2}O_2$) to provide a cerium-based support with distinct intrinsic properties. The Zr-rich complex oxide is claimed to stabilize high contents of Pr^{3+}, thus favoring the formation of oxygen vacancies [14,16]. Moreover, the Pr^{3+} site could act as Lewis basic site to stabilize added acidic component (W and Nb, see below) and possibly trap NO$_x$ species. The choice of this specific praseodymium loading comes from the satisfactory compromise between the interesting redox properties due to the presence of about 50 % of Pr^{4+} [16].

Additionally, acidic behaviors are required for NH$_3$-SCR catalysts to adsorb and activate ammonia. Among the acidic oxides other than V_2O_5, WO_3 and Nb_2O_5 are particularly popular for this application. WO_3/CeO_2-ZrO_2 was reported as an attractive SCR catalyst in 2008 by Li et al. [17]. The tungsten addition to CeO_2-ZrO_2 induces the inhibition of the CeZr basic sites for the benefit of acidic surface sites [18]. More recently, it was showed that WO_3 favors the reduction of Ce^{IV} into Ce^{III} and then promotes the low-temperature SCR activity [19]. Chen et al. proposed that the tungsten-cerium interactions may favor the activation of gaseous oxygen to compensate the lattice oxygen consumed by the NH$_3$-SCR reaction at low temperature (200 °C) [20]. Nevertheless, it was also reported that a high WO_3 loading on CeO_2 could induce a decrease in the SCR activity due to the formation of $Ce_1W_2O_x$ species [21].

Niobium oxide on ceria also exhibits strong beneficial interactions. Single niobium oxide or ceria are nearly no active alone in NH$_3$ SCR but supported Nb_2O_5/CeO_2 catalysts exhibit high NO$_x$ conversion rate, from 200−250 °C [22]. Qu et al. indicated that both Lewis and Brønsted acid sites from niobium oxide are involved in the low-temperature activity, while only the Lewis acid sites (LAS) contribute to the SCR reaction at high temperature [22]. The Nb-Ce synergetic interaction was also evidenced in Nb_2O_5-CeO_2/WO_x-TiO_2 systems; the NO$_x$ conversion was significantly improved compared to CeO_2/WO_x-TiO_2 for both low and high temperatures ranges [23]. On ceria-zirconia, Ma et al. proposed that acidic NbO$_x$ species also enhance the Lewis acid sites on CeZr surface by attracting electrons. Consequently, it promotes the NH$_3$ adsorption and inhibits the undesired NH$_3$ oxidation into NO$_x$. Moreover, authors suggested that the increase of oxygen active species over NbO$_x$/CeZr promoted both the adsorptive oxidation of NH$_3$ to NH$_2$ and NO to NO_3^- [24]. Interestingly, Lian et al. showed that the addition of Nb on VO_x/CeO_2 systems not only improved the acidic behavior, but also enhanced the NO$_x$ adsorption capacity [25]. A Langmuir-Hinshelwood mechanism was then proposed in which adsorbed NO$_x$ species reacted with adsorbed NH$_3$, whereas an Eley-Rideal type mechanism is commonly accepted, involving a nitrosamine (NH$_2$NO) intermediate species [26]. As for tungsten, niobium was reported to improve the redox behavior of CeZr oxides, due to the formation of oxygen vacancies, because of the interaction between Ce^{n+} and Nb^{n+} [27]. However, the stabilization of W^{6+} and Nb^{5+} species with valence states higher than 4+ observed in ceria-zirconia shows the occurrence of highly complex structural defects involving oxygen vacancies mainly surrounding transition metals (W, Nb) and consequently over-coordinated Ce^{4+}/Ce^{3+} (coordination number > 8, with enhancement of the Lewis basic character) in regard to the oxygen over-stoichiometry.

Finally, to get insights in the NH$_3$-SCR reaction pathways and especially toward the competitive ammonia oxidation, a $Ce_{0,2}Zr_{0,8}O_2$ support have been selected modified by the partial substitution of zirconium for praseodymium ($Ce_{0,2}Zr_{0,6}Pr_{0,2}O_2$). Both supports were impregnated with tungsten or niobium salts to obtain significant differences in the redox and acidic properties of the catalysts, allowing the establishment of proper reaction pathways.

2. Experimental part

2.1. Catalysts preparation

$Ce_{0,2}Zr_{0,8}O_2$ and $Ce_{0,2}Zr_{0,6}Pr_{0,2}O_2$ supports, denoted CZ and CZP, respectively, were synthetized by coprecipitation at pH = 10 from nitrate precursors. After a maturation step at room temperature for 4 h, the precipitate was washed six times with a diluted ammonia aqueous solution (M/100) and twice with ethanol. After drying at 50 °C under air, the sample was annealed in air at 700 °C for 12 h. Finally, the solid was calcined under wet air (10 % H_2O) during 12 h at 600 °C.

Both supports were impregnated with niobium and tungsten salts to obtain approximately 9 $_{wt}$%. Tungsten was added by impregnation of the corresponding amount of ammonium metatungstate $(NH_4)_{10}W_{12}O_{41}.5H_2O$ diluted in water. This addition was performed at 60 °C under continuous agitation. The preparation was then dried at 80 °C and placed in an oven at 120 °C for a night before calcination at 600 °C for 4 h (5 °C min^{-1}) in a muffle furnace. Finally, the solid was treated under wet air (10 $_{vol}$% H_2O) during 12 h at 600 °C. The obtained catalysts are noted W/CZ and W/CZP depending on the support composition.

For niobium impregnation, the desired amount of $NbCl_5$ was firstly diluted in ethanol at 45 °C and then mixed with the support previously dispersed in ethanol [28] because $NbCl_5$ reacts with water [29]. The resulting solution was placed on a stirring plate overnight. Solvent was then evaporated on a sand bath, and the obtained powder was submitted to the same treatments as WO_3 based samples: one night drying at 120 °C, calcination at 600 °C for 4 h, and hydrotreatment at 600 °C for 12 h. The resulting samples are denoted Nb/CZ and Nb/CZP.

The samples were sieved, and the fractions 100–250 µm were used for tests and analyses.

2.2. Physical and textural properties, elemental analysis and magnetic susceptibility

Nitrogen adsorption-desorption isotherms were recorded at –196 °C, using a Tristar 3000 Micromeritics apparatus. Prior to the measurement, the samples were pretreated at 250 °C under vacuum for 8 h. The surface area was calculated using the BET model, the pore volume is evaluated at P/P_0 = 0.97, and the pore diameter was evaluated using the BJH model applied to the desorption branch of the isotherms.

Powder X-ray diffraction (XRD) patterns were recorded on a PANalytical X'Pert MPD apparatus with Bragg − Brentano geometry using a monochromated Cu K_α radiation (λ = 1.54059 Å) for accurate studies and an X'Celerator detector. Data were collected over a range of 10°-80° with 0.017° steps (60 s counting time). The lattice parameters and the crystallite sizes were determined by profile matching (Le-Bail fit) using the Thomson-Cox-Hastings function with the JANA2006 program package. Crystalline phases were identified by comparison with ICDD database files.

Elemental analyses were carried out to assess the niobium and tungsten loadings. After mineralization of the samples, analyses were performed with an ICP-OES apparatus (Agilent 5110S).

The thermal variation of the magnetic susceptibility χ (T) = M/H, was recorded using a MicroSense EZ7 vibrating magnetometer in order to estimate the valence state of Praseodymium (Pr^{4+} ($4f^1$) and Pr^{3+} ($4f^2$) considering that in complex oxides annealed under air, diamagnetic Ce^{4+} ($4f^0$) ions are stabilized. Magnetization (M) has been recorded between 220 and 370 K (speed rate: 10 °C/min) in a magnetic field (H) of 18 000 Oe. The Curie constant (C) and Weiss temperature (θp) were deduced from magnetic susceptibility measurements ($1/\chi = (T+\theta p)/C$ which follows a Curie-Weisss law). As the Curie constant is proportional to the concentration of the paramagnetic species, the $Pr^{3+}(4f^2)$ (effective magnetic momentum μ_{eff} = 2.54 μ_B) and $Pr^{4+}(4f^1)$ (effective magnetic momentum μ_{eff} = 3.58 μ_B) contents in the various compounds can be deduced from magnetic data. Results are presented in the Supplementary Information (SI) file, section 2.

2.3. Acidic properties

2.3.1. NH_3 storage

Acidic properties were carried out by dynamic ammonia storage measurements at 200, 300 and 400 °C. Before analysis, the catalyst (100 mg + 100 mg SiC) was pretreated *in situ* for 30 min at 500 °C under a 10 % CO_2, 8 % H_2O and N_2 gas

mixture (total flow rate: 20 $L.h^{-1}$), and cooled down to the desired storage temperature under the same mixture. The sample was then submitted to a flow containing 400 ppm NH_3, 10 % CO_2, 8 % H_2O and N_2 previously prepared in by-pass (Table 1, total flow rate: 20 $L.h^{-1}$) until ammonia signal reached 400 ppm (saturation of the catalyst) again. The ammonia storage capacity was estimated by the integration of the recorded profile. The contribution of the reactor volume was measured for each temperature using only SiC as catalytic bed, and subtracted to the obtained profiles. The gas mixture was imposed by mass-flow controllers, except for H_2O which was introduced *via* a saturator. All gases, except diatomic gases, were followed by MKS 2030 Multigas infrared analyzer. Therefore, these NH_3 storage capacity measurements are carried out under experimental conditions close to the SCR media.

Table 1
NH_3 storage and catalytic test gas composition. 100 mg catalyst +100 mg SiC, total flow rate: 20 L h^{-1}.

Catalytic test/gas mixture	NH_3	NO	O_2	CO_2	H_2O	N_2
NH_3 storage	400 ppm			10 %	8 %	Balance
NH_3-SCR	400 ppm	400 ppm	10 %	10 %	8 %	Balance
NH_3-SCO	400 ppm	–	10 %	10 %	8 %	Balance
NO oxidation		400 ppm	10 %	10 %	8 %	Balance

2.3.2. NH_3 adsorption followed by infrared spectroscopy

The surface acidity of the supported WO_3 and Nb_2O_5 samples on CZ and CZP was evaluated by ammonia adsorption monitored by FTIR. Spectra were collected with a Nexus Nicolet spectrometer equipped with a DTGS detector (Deuterium TriGlyceride Sulfur) and KBr beam splitter. Data were recorded with a resolution of 4 cm^{-1} and 64 scans.

The adsorption of NH_3 (500 Pa at equilibrium) is carried out at room temperature after activation of the sample in synthetic air at 500 °C for 12 h, followed by a secondary vacuum step at 300 °C.

Desorption was performed up to 450 °C, by temperature step of 50 °C. The presented spectra were normalized to a disc of 10 mg cm^{-2}.

2.4. Redox properties

2.4.1. Temperature programmed reduction with hydrogen (H_2-TPR)

Temperature programmed reduction (TPR) experiments were performed on a Micromeritics Autochem 2920 apparatus equipped with a thermal conductivity detector (TCD). Catalyst (150 mg) was placed in a U-shape quartz reactor. Before the measurement, the sample was calcined at 600 °C for 120 min under 10 vol.% O_2 in Ar flow (temperature increase rate: 5 °C min^{-1}). The sample was cooled down to room temperature and purged under Ar flow for 45 min. The reduction was carried out under 10 vol.% H_2 in Ar flow up to 1000 °C (temperature rate: 5 °C min^{-1}). H_2O-trap was added downstream of the reactor because the TCD signal is sensitive to water.

2.4.2. Oxygen storage capacity (OSC/OSCC)

The oxygen storage capacity measurements were carried out in an atmospheric U-shape quartz fixed bed reactor connected to a TCD. Experiments were performed at various stabilized temperature between 400 and 600 °C. The sample (20 mg) was continuously purged with helium (30 $mL.min^{-1}$). After oxidation with pure O_2 pulses, the sample was submitted to CO pulses (465 µL) every 2 min until CO consumption and CO_2 emission were nil [30]. A series of O_2 pulses is finally added for sample reoxidation. The oxygen storage capacity (OSC) was calculated from the first CO pulse while the oxygen storage capacity complete (OSCC) value was evaluated at the end of the CO pulses series. The OSCC value corresponds to the total amount of reactive oxygen, whereas OSC corresponds to dynamic availability and reactivity of oxygen species. The amounts of unconverted CO and O_2 as well as of produced CO_2 were quantified. The OSC/OSCC was calculated from the value of CO_2 production (after CO pulse(s)) and was expressed in $\mu mol_O/g$. On ceria-based supports, the values related to CO consumption could lead to overestimated OSC values due to formation

of carbonates by the reaction of CO with surface basic oxygen species, as previously reported [31,32]. Some authors also reported that part of the CO_2 production could be due to gas-phase reaction of CO disproportionation promoted by the presence of Ce^{3+} [33]. To remove any doubt on the OSCC values, the amount of O_2 consumed during the final re-oxidation step was also considered.

2.4.3. Isotopic exchange

Oxygen isotopic exchange experiments were performed in a U-form reactor placed in a closed recycle system (total volume: 70 mL) connected to a mass spectrometer (Pfeiffer Vacuum, QMS 200) for the monitoring of the gas phase composition and to a vacuum pump. The recycling pump placed in the system removes limitations due to gas-phase diffusion (recirculation rate: 170 $cm^3\ s^{-1}$). The sample (20 mg) was first exposed to pure $^{16}O_2$ at 600 °C for 1 h prior to cooling at desired temperature for isothermal oxygen isotopic exchange (IOIE) experiments. This step ensures that the material surface is free from adsorbed species such as carbonates, which could influence the oxygen-exchange activity. The system was thereafter purged for 30 min under vacuum and then charged with 55 mbar of $^{18}O_2$ (Eurisotop, 97.4 % ^{18}O). The masses *m/z* = 32, 34, and 36, which correspond to $^{16}O_2$, $^{18}O^{16}O$, and $^{18}O_2$, respectively, were monitored continuously. The *m/z* value of 28 (N_2) was also recorded to detect possible leaks in the experimental system. The methods used to calculate the atomic fraction of ^{18}O in the gas-phase (α_g) and the initial rate of exchange (V_e) as described previously in [34] where *Ng* is the total number of oxygen atoms in the gas phase.

Typically:

$\alpha_g = \frac{\frac{1}{2}P_{34} + P_{36}}{P_{32} + P_{34} + P_{36}}$ in %, where P_{32}, P_{34}, P_{36} are the partial pressures of $^{16}O_2$, $^{16}O^{18}O$ and $^{18}O_2$ respectively;

$V_e = -N_g \frac{d\alpha_g}{dt}$ in at/g/s.

2.5. Catalytic tests: NH_3-SCR tests, NH_3-SCO and NO oxidation

The selective catalytic reduction (SCR) activity measurement was carried out in a quartz tubular micro-reactor under a flow simulating realistic lean exhaust conditions depicted in Table 1. The catalyst (100 mg) was diluted with 100 mg SiC and the total flow rate was fixed at 20 L h^{-1}, corresponding to a GHSV of about 160 000 h^{-1} (GHSV, calculated as the volume of feed gas/volume of catalyst). The gas mixture was imposed by electronic mass-flow controllers, except for H_2O which was introduced *via* a saturator. The compositions of the feed gas and effluent stream were monitored continuously using online MKS 2030 Multigas infrared analyzer. Conversions were typically calculated by Eq. (3)

$$\text{Conversion}_X\ (\%) = ([X]_{inlet} - [X]_{outlet})/[X]_{inlet} \times 100 \qquad (3)$$

The N_2 selectivity was calculated assuming no other N-compounds than NO, NO_2, N_2O and NH_3 are formed.

The selective catalytic oxidation (SCO) of NH_3 was carried out using similar protocol as previously depicted for SCR test, except that NO was replaced by the same flow of nitrogen (Table 1). Besides, NO oxidation behavior activities were also evaluated, using likewise similar protocols as for SCR tests, except that NH_3 was replaced by the same nitrogen flow (Table 1).

3. Results and discussion

3.1. Chemical composition, textural and structural properties

3.1.1. Textural properties and chemical composition

The $Ce_{0,2}Zr_{0,8}O_2$ support (CZ) exhibited a specific surface area of 25 $m^2\ g^{-1}$ after the hydrotreatment ageing at 600 °C for 12 h (Table 2). This surface area was slightly affected after impregnating niobium or tungsten oxide and after the subsequent treatments described in section 2.1, reaching 22 and 20 $m^2\ g^{-1}$, respectively. The chemical analysis by ICP

of supported CZ catalysts indicated loadings of 8.1 $_{wt}$% Nb and 8.4 $_{wt}$% W, corresponding to 11.6 $_{wt}$% Nb_2O_5 and 10.6 $_{wt}$% WO_3, respectively.

The partial praseodymium substitution for zironium ($Ce_{0,2}Zr_{0,6}Pr_{0,2}O_2$) led to a moderate increase of the specific surface area compared to CZ, at 32 $m^2\ g^{-1-}$, but the impact of Nb (8.5 $_{wt}$%) or W (9.7 $_{wt}$%) impregnation was more significant, leading to surface areas of 27 $m^2\ g^{-1}$ and 22 $m^2\ g^{-1}$, respectively. Finally, the four supported studied catalysts (W/CZ, Nb/CZ, W/CZP and Nb/CZP) showed specific surface area in the 20–27 $m^2\ g^{-1}$ range (Table 2).

Table 2
Specific surface area, W or Nb loading (ICP analysis), structural and textural characteristics of studied samples.

	CZ	CZP	Nb/CZ	Nb/CZP	W/CZ	W/CZP
S_{BET} ($m^2\ g^{-1}$)	25	32	22	27	20	22
$_{wt}$% (Nb)	–	–	8.1	8.5	–	–
$_{wt}$% (W)	–	–	–	–	8.4	9.7
support cell parameters (Å)	5.233 (3)	5.258 (2)	a = 3.643 (2) c = 5.236 (3)	5.242 (3)	a = 3.645 (2) c = 5.231 (2)	5.238 (2)
T-Nb_2O_5 or *m*-WO_3 "a, b, c" cell parameters (Å) and β angle (deg)	–	–	a = 6.236 (2) b = 29.190 (3) c = 3.914 (3)	a = 6.132 (3) b = 29.018 (3) c = 3.830 (3)	a = 7.311 (3) b = 7.524 (3) c = 3.846 (2) β = 90.679 (3)	a = 7.311 (3) b = 7.524 (3) c = 3.846 (2) β = 90.679 (3)
support crystallite size (nm)	7 (1)	6 (1)	12 (1)	5 (1)	13 (1)	6 (1)
T-Nb_2O_5 or *m*-WO_3 crystallite size (nm)	–	–	2 (1)	8 (1)	6 (1)	6 (1)

Values in brackets correspond to the uncertainty attributable to last given digit.

3.1.2. Structural properties

XRD patterns (Fig. 1) of CZ and CZP compounds revealed pure phases which crystallize with the fluorite-type structure. Full pattern matching refinement of XRD data (Le-Bail fit, Fig. S1) revealed a slight increase of unit cell parameter (from 5.223 Å to 5.258 Å) after Pr substitution in CZP compound (Table 2), despite the high content of large Pr^{3+} cation (around 40 %, determined by magnetic measurement, SI file section 2). The ionic radii of each species (in coordinence 8) is given as follow: Pr^{3+}: 1.126 Å; Ce^{4+}: 0.97 Å; Pr^{4+}: 0.96 Å; Zr^{4+}: 0.84 Å. The refined crystallite size (Thomson-Cox Hastings model) remained identical, at around 7(1) nm whatever the composition. Nb_2O_5 and WO_3 loading in CZ led to a tetragonal distortion ($P4_2/nmc$ space group) of the previous fluorite network and the crystallite size increased up to 13(1) nm. Note that a decrease of 2.3 % of the unit cell volume per formulae unit (V/Z) was also observed after Nb_2O_5 or WO_3 addition (Table 2), which would correspond to an increase in the Zr/Ce atomic ratio. Other weak XRD peaks were also detected, marked with stars in Fig. 1, which correspond to *T*-Nb_2O_5 (orthorhombic *Pbma* Nb_2O_5-type phase) and monoclinic *m*-WO_3 ($P2_1/a$ space group). Full pattern profile matching have been carried out on these samples (Fig. S1, Supporting Information file). It revealed the presence of two well indexed phases. The slight deviation of *T*-Nb_2O_5 and *m*-WO_3 unit-cell parameters from pure binary oxides combined with the stabilization of the tetragonal form of the fluorite-type structure could be attributed to the partial incorporation/substitution of Ce^{4+} in *T*-Nb_2O_5 and *m*-WO_3 oxides. The same approach has been undertaken for CZP supported catalysts and the same sequence of additional peaks also appeared. The main diffraction lines still corresponded to the cubic symmetry and fluorite network. The V/Z change after Nb_2O_5 or WO_3 loading was very low in this case, at around 0.4 % *vs.* 2.3 % for CZ supported samples. Furthermore, the crystallite size did not vary after Nb_2O_5 or WO_3 addition on CZP. The highest phase purity was observed for m-WO_3/CZP sample (Fig. S1).

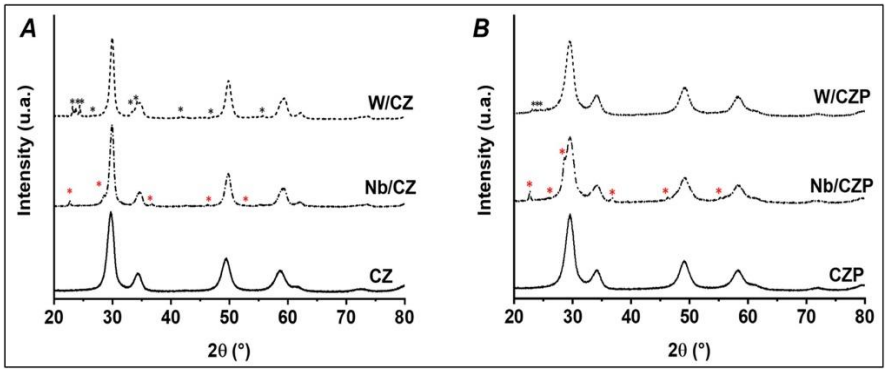

Fig. 1. Powder XRD patterns of (A): CZ-based catalysts and (B): CZP-based catalysts. (*): undetermined additional phases.

3.2. Total reducibility assess by H_2-TPR and OSCC experiments

The total reducibility behavior of the samples was studied by two different techniques, namely the temperature programmed reduction with hydrogen (H_2-TPR) and complete oxygen storage capacity (OSCC) measurement, estimated by pulses of CO at stabilized temperature.

3.2.1. H_2-TPR

The H_2-TPR was used to investigate the reduction behaviors of materials and also to assess to the initial redox state of the elements.

The TPR curve of the CZ support showed a typical profile of ceria-zirconia mixed oxides reduction (Fig. 2A). The reduction started near 300 °C and the main peak, centered at 606 °C, was recorded until 680 °C. The complete reduction was not reached at this temperature since a new small reduction peak started to appear near 900 °C. The total H_2 consumption of CZ material recorded after stabilization at 1000 °C for 30 min was 748 $\mu mol_{H2}\ g^{-1}$ (Table 3). Based on the ceria reduction equation ($2CeO_2 + H_2 \rightarrow Ce_2O_3 + H_2O$), almost all Ce^{IV} species were reduced into Ce^{III}.

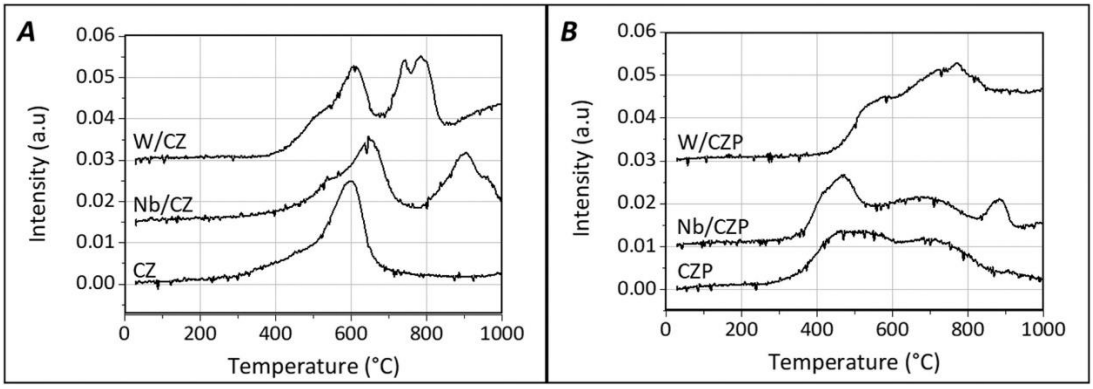

Fig. 2. TPR profiles of (A): CZ-based catalysts and (B): CZP-based catalysts.

After niobium impregnation, the main reduction peak of CZ was shifted by approximately 60 °C to higher temperature (starting temperature and maximum). A second reduction peak was recorded in the 800−1000 °C temperature range. This peak was related to the reduction of Nb_2O_5 species into Nb_2O_4 [35]. The experimental H_2 consumption related to the niobium oxide reduction (460 $\mu mol_{H2}\ g^{-1}$) is close to the expected value for Nb^{V} reduction into Nb^{IV} reduction (436 $\mu mol_{H2}\ g^{-1}$) based on the niobium loading measured by ICP (8.1 %). Moreover, the theoretical H_2 consumption to reduce Ce^{IV} in Nb/CZ was calculated at 665 $\mu mol_{H2}\ g^{-1}$, while the integration of the first reduction peak until 800 °C, attributed to Ce^{IV} reduction, led to the consistent value of 638 $\mu mol_{H2}\ g^{-1}$ (+3.6 % overestimation, Table 3). Consequently, Nb impregnation delayed the support reduction temperature but it did not impact the percentage of reducible cerium species.

Addition of WO_3 on CZ strongly shifted the starting temperature of the support reduction from 300 °C to 400 °C, whereas a minor shift of 6 °C was observed for the maximum peak temperature (from 606 °C to 612 °C). At higher temperature, H_2-TPR profile revealed a second broad H_2 consumption with two maxima in the 700−850 °C temperature range, while a new slow H_2 consumption started from 850 °C. The hydrogen consumption for temperature higher that 700 °C is related to WO_3 reduction [36]. The recorded H_2 consumption related to the tungsten oxide reduction (1196 $\mu mol_{H2}\ g^{-1}$) was slightly lower than the calculated value for the reduction of 8.4 % WO_3 into W (1370 $\mu mol_{H2}\ g^{-1}$). However, the TPR profile of W/CZ indicated that the tungsten oxide reduction was probably not fully completed at 1000 °C, and it could also be consistent with the fact that tungsten trioxide usually exhibits vacancies and is denoted WO_{3-x}. The H_2 consumption related to the first reduction peak of W/CZ and assigned to the reduction of Ce^{IV} species into Ce^{III} (674 $\mu mol_{H2}\ g^{-1}$, Table 1) was very close to the theoretical total Ce^{IV} reduction (672 $\mu mol_{H2}\ g^{-1}$ taking into account that the catalyst also contained WO_3 oxide), showing that W addition had no influence on the amount of reducible cerium under H_2, as previously observed [18], but it delayed the beginning of the CZ support reduction in a higher extent than niobium.

Table 3
Redox properties: TPR tests (total H_2 consumption ($\mu mol_{H2}\ g^{-1}$); OSC/OSCC results ($\mu mol_O\ g^{-1}$), measured by CO pulses at stabilized temperature.

Technique		CZ	CZP	Nb/CZ	Nb/CZP	W/CZ	W/CZP
TPR H_2 cons. ($\mu mol_{H2}\ g^{-1}$)	20–1000 °C	748	1134	1098	1215	1870	2028
	20 - 400 °C	40	72	5	50	3	1
	peak 1		601	638		674	
	peak 2		533	460			
OSCC ($\mu mol_O\ g^{-1}$)	400 °C	206	128	27	52	0	0
	500 °C	521	316	73	100	7	0
	600 °C	733	500	129	150	20	19
OSC ($\mu mol_O\ g^{-1}$)	400 °C	84	39	10	7	0	0
	500 °C	196	122	28	36	2	0
	600 °C	377	244	46	72	7	6
Initial rate of isotopic oxygen exchange (10^{19} at. $g^{-1}.s^{-1}$) at 500 °C		6.23	34.40	0.56	4.52	0.85	1.57

Compared to CZ material, the partial praseodymium substitution for zirconium ($Ce_{0,2}Zr_{0,6}Pr_{0,2}O_2$, Fig. 2B) decreased the starting reduction temperature, from 300 °C for CZ to approximately 250 °C for CZP but both profiles appeared very similar until 370 °C. However, CZP exhibited a more intense H_2 consumption in the 370–520 °C temperature range, which is probably related to the reduction of Pr^{IV} species [37]. The two main reduction peaks of the CZP TPR profile were recorded at 475 °C and 690 °C and the total H_2 consumption was 1134 $\mu mol_{H2}\ g^{-1}$ after stabilization at 1000 °C (Table 3). Praseodymium in CZ then favored both the amount of reducible species before 520 °C and the total amount of reducible species as mentioned in literature [14,16]. In addition, the theoretical H_2 consumption corresponding to the full reduction of Ce^{IV} species into Ce^{III} in CZP support is 700 $\mu mol_{H2}\ g^{-1}$. The same amount would be necessary to reduce Pr^{IV} species into Pr^{III}. In accordance to the quantification of the CZ TPR experiment, the assumption of a full reduction of Ce^{IV} species into Ce^{III} at 1000 °C can be postulated. Consequently, only 436 $\mu mol_{H2}\ g^{-1}$ were attributed to praseodymium reduction. Since Pr^{IV} species reduction by H_2 is commonly observed in the 200−500 °C temperature range [38], it suggests that praseodymium was not only in Pr^{IV} state before the TPR experiment, but a part (38 %) was already in Pr^{III} state. This assumption is supported by the magnetic susceptibility measurements which revealed that 43 % of the praseodymium was detected as Pr^{3+} in CZP (SI file, section 2).

Niobium addition on CZP led to a shift of reduction start, from 250 °C (CZP) to 350 °C (Nb/CZP). The two reduction peaks of the CZP support were still observed and a third peak, centered at 890 °C and related to niobium oxide reduction, was recorded. A fourth peak started near 950 °C. The impact of tungsten addition on CZP reduction behavior was more marked. Furthermore, note that XRD pattern of W/CZP sample revealed the lowest intensities of additional (non-indexed) peaks in this series, leading to consider the strong interactions of W^{6+} ions with fluorite matrix despite the almost similar unit-cell parameters of CZP compounds with or without W. The beginning of the reduction was dramatically shifted from 250 °C to 450 °C and the maximum of the first peak was recorded at 585 °C, corresponding to a shift of approximately 85 °C compared to the support alone. The second reduction peak, including both the second CZP reduction step and the tungsten oxide reduction, was recorded at 775 °C. A third reduction peak started after 950 °C. This profile demonstrates strong interactions between W and Pr^{III}/Pr^{IV} compared to Nb/CZP sample. Concerning the H_2 consumptions assigned to the reduction of Nb_2O_5 or WO_3, they were difficult to exploit due to the late reduction of the bare support in the same temperature range.

3.2.2. OSCC

To obtain more information on the reducibility behaviors, the samples were also characterized by OSCC measurement (Table 3). This technique differs from TPR measurement by both the reductant agent (CO) and the protocol, since the sample was submitted to short pulses of pure CO at stabilized temperature between 400 and 600 °C. In order to compare both techniques, the TPR profiles were integrated in the 20−400 °C temperature range to assess the more reducible species (Table 3). This temperature range was also selected in regards of the catalytic test (section 3.5). As expected, the OSCC values increased with temperature. For CZ support, 98 % of Ce^{IV} was reduced into Ce^{III} at 600 °C. In opposition with the TPR experiments, the CZP support exhibited lower OSCC than the CZ support, whatever the studied temperature. The reducibility of CZP support appeared then strongly dependent on the used techniques, namely H_2-TPR and OSCC measurements, because this two reductant species involve different reduction mechanisms. It also induces that the total amount of reactive oxygen toward CO is lower over CZP sample than on CZ.

The Nb addition on CZ induced a strong decrease in OSCC, with loss of 87 %, 81 % and 80 % at 400 °C, 500 °C and 600 °C, respectively, while the H_2 consumption in the 20−400 °C temperature range of TPR was decreased by 87 %, from 40 $\mu mol_{H2}\ g^{-1}$ to 5 $\mu mol_{H2}\ g^{-1}$ (Table 3). Nb/CZP showed slightly higher OSCC values than Nb/CZ whereas the H_2 consumption in the 20−400 °C temperature range showed a ten time higher value (50 $\mu mol_{H2}\ g^{-1}$). The inhibiting effect of tungsten addition on OSCC was even more significant than for niobium. No reduction by CO was observed at 400 °C on W/CZ and W/CZP, and the OSCC values measured at 500 and 600 °C remained very low, between 0 and 20 $\mu mol_{CO}\ g^{-1}$. The characterization by H_2-TPR showed the same trends since the reduction of W based catalysts was not significant before 400 °C (Table 3).

Finally, the reactivity of the samples toward H_2 and CO significantly differed. In general, H_2 appeared a better reductant agent than CO, and opposite variations can be observed depending on the reductant species, as observed for the supports: the partial substitution of praseodymium for zirconium favors the sample reduction of the mixed oxide under H_2 in the 20−400 °C temperature range, but the OSCC measured with CO was decreased (-38 % at 400 °C). It could be attributed to the occurrence of Pr^{3+} as Lewis basic centers, which would contribute to limit CO adsorption. Whatever the characterization technique, both Nb and W were found to strongly inhibit the low-temperature reduction. The reduction by H_2 was delayed to 350 °C after Nb addition for both supports, while the OSCC values were decreased by 80 % in the 400−600 °C temperature range. The inhibiting effect of W was even more marked, especially on CZP support. The H_2 consumption in the 20−400 °C range was decreased from 40 to 3 $\mu mol_{H2}\ g^{-1}$ on CZ, and from 72 to 1 $\mu mol_{H2}\ g^{-1}$ on CZP. Simultaneously, the OSCC values measured in the 400−600 °C temperature range became nil or very low.

3.3. Dynamic redox properties assess by isotopic $^{18}O_2$ exchange and OSC experiments

3.3.1. $^{18}O_2$ isotopic exchange

Redox behaviors could be also described by the ability of the sample to exchange oxygen from the gas phase with lattice oxygen atoms. Although the sample reduction does not occur in the exchange mechanism, a close relationship between the reducibility measured by CO-OSC and O mobility determined by Oxygen Isotopic Exchange was already reported on three-way catalysts [39]. Fig. 3 shows the ^{18}O concentration profiles plotted as a function of time on stream during the isotopic exchange experiments at 500 °C (recirculation of the gas mixture, initially composed of 97 % $^{18}O_2$). The comparison between both bare CZ and CZP supports clearly evidenced that the partial substitution of Pr for Zr improved the oxygen exchange process with the initial exchange rate multiplied by more than 5 (Table 3). However, Nb or W impregnation strongly inhibited this behavior since a decrease of one order of magnitude was generally observed. Specifically, the oxygen exchange rate became very slow on both supports after tungsten addition, while niobium oxide impact was found to be more severe on CZ than on CZP (Fig. 3, Table 3).

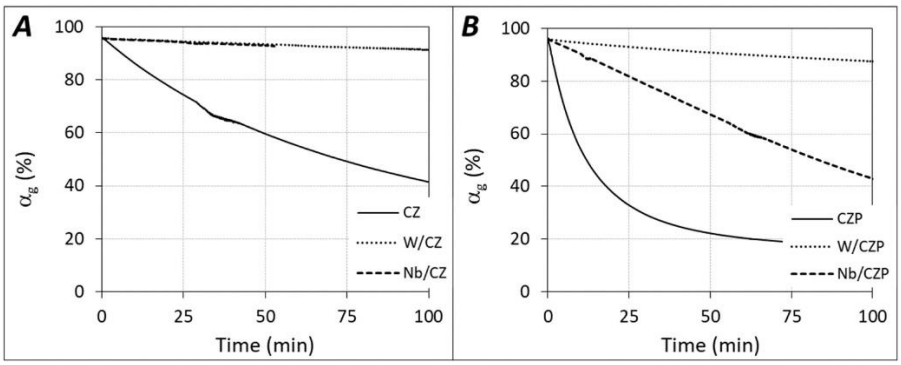

Fig. 3. Evolution of the the atomic fraction of ^{18}O in the gas-phase (α_g) (%) depending on time on stream (recirculation at 500 °C of the gas mixture initially composed of 97 % $^{18}O_2$) of (A): CZ-based catalysts and (B): CZP-based catalysts.

3.3.2. OSC

OSC data depending on temperature are reported in Table 3. These results highlight the dynamic surface O_2 reactivity compared to OSCC measurements. Overall, oxygen storage capacity increase with temperature. The main differences are observed for Nb-containing samples. In fact, higher OSC values were reported for Nb/CZP support compared to Nb/CZ. Compared to OSCC measurements, it induces that Pr substitution for Zr maintained surface oxygen availability after Nb deposit. To the opposite, OSC measurements are nil for W-containing catalysts, which is in agreement with OSCC experiments. Overall, it highlights again the strong interaction of W with Pr^{IV}, in accordance with TPR profiles reported in Fig. 2B.

3.4. Acidic properties

Acidic properties were evaluated by both NH_3 storage capacities measurement at stabilized temperature and ammonia adsorption monitored by FTIR.

All the obtained NH_3 profiles are compared in Fig. S3 (Supplementary Information file). The profile obtained with inert SiC described the purge of the reactor. The CZ sample exhibited nearly no ammonia storage at 200 °C and 300 °C (Table 4) and the baseline corresponding to 400 ppm NH_3 was recovered in approximately 90 s. This result is consistent with the fact that the presence of acidic sites was not expected over ceria-based samples. At 400 °C, the first part of the NH_3 profiles tended to be similar to the reactor purge but the baseline appeared not fully recovered. Same tendencies, but more significantly marked, were observed with CZP sample, as illustrated in Fig. 4A: the NH_3 outlet concentration at 400 °C was stabilized near 350 ppm after the reactor purge step. This constant value was observed during all the measurement duration (20 min, not shown). Consequently, NH_3 is supposed to be able to reduce the CZ at $T \geq 400$ °C and CZP at $T \geq 300$ °C. Indeed, TPR and OSC experiments showed that CZ and CZP supports can be reduced either by H_2 or CO in this temperature range. Moreover, NH_3 oxidation experiments (SCO) showed that both supports are able to oxidize ammonia below 350 °C (see thereafter section 3.5.1, Fig. 5C1). Then, the assumption of the support reduction when submitted to NH_3 is highly plausible. Accordingly with TPR and OSC experiments which showed that Nb_2O_5 or WO_3 addition inhibited the support reduction, baseline was also rapidly recovered during the ammonia storage tests. Note that (i) no NO_x emission was recorded during the ammonia storage tests and (ii) considering a constant NH_3 consumption of 50 ppm, approximately 2 h under stream would be necessary to reduce Ce^{IV} and Pr^{IV} in CZP. When NH_3 baseline was not recovered for CZ and CZP support, the integration of the profiles cannot be trustingly exploited. However, the ammonia storage capacities can be supposed become nil with the increase of the temperature test since the NH_3 storage was very low at 200 °C.

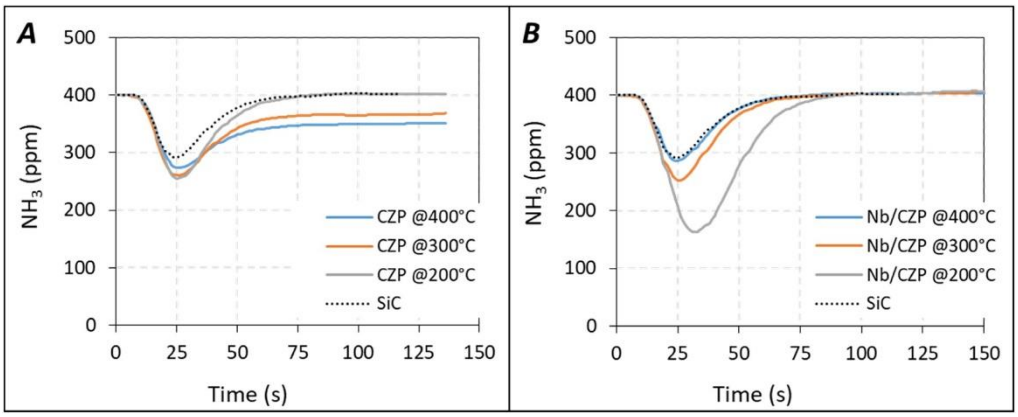

Fig. 4. NH_3 storage capacity measurements depending on the temperature. NH3 outlet profiles recorded with A: CZP support; B: Nb/CZP sample. All profiles are available in the Supplementary Information file.

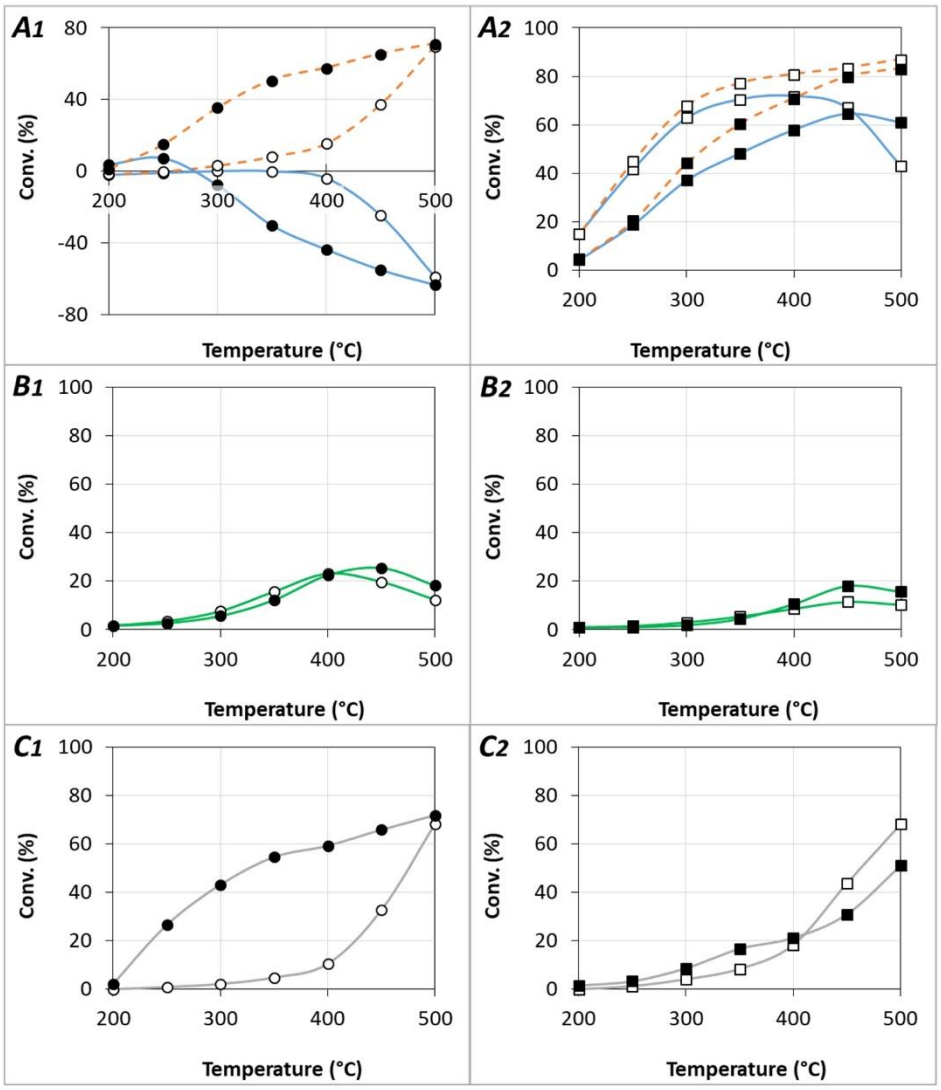

*Fig. 5. Catalytic performances of **1**-CZ (○, open symbol) and CZP (●, full symbol) supports and **2**-Nb-supported catalysts (Nb/CZ: □, open symbol; Nb/CZP: ■, full symbol) in A: NH_3-SCR (NOx conversion: ▬, full blue line; NH_3 conversion: - -, dotted orange line); B: NO oxidation (▬); C: NH_3 oxidation (▬).*

Whatever the support, after Nb or W addition, the NH_3 profiles always rapidly recovered the initial NH_3 concentration of 400 ppm. The maximum equilibrium time was nearly 150 s, recorded with W/CZ at 200 °C. These results obtained with NH_3 are in accordance with results previously reported in section 3.2: CZP support appeared more reducible than CZ, while Nb and W addition inhibited the support reduction by H_2 or CO as reductant agent.

As expected, the ammonia storage capacities were enhanced by the addition of tungsten or niobium as illustrated in Fig. 4B, but the obtained storage capacities remained generally low (Table 4). On CZ, W addition led to double NH_3 storage capacities compared to Nb. The NH_3 adsorption capacities were lowered on CZP, and both Nb and W containing catalysts showed similar results. Then, praseodymium inhibited the ammonia adsorption on Nb_2O_5 and on WO_3 in a higher extent.

Table 4
NH_3 storage capacities (μmol g^{-1}).

Temperature (°C)	CZ	CZP	Nb/CZ	Nb/CZP	W/CZ	W/CZP
200	2.0	1.5	10.6	11.0	21.8	11
300	0.4	*	8.0	2.1	17.3	2.9
400	*	*	1.9	0.6	7.1	0.3

* Integration of the profile cannot be trustingly exploited because the baseline was not recovered (reduction of the sample).

Acidity was also evaluated by NH_3 adsorption monitored by FTIR in order to assess to the nature of the acid sites (Lewis *vs.* Brønsted). In fact, NH_3 adsorption results in complex IR bands in the 3500−3000 cm^{-1} spectral range of N—H stretching vibration modes due to a splitting of the $\nu_{N-H,asym}$ mode and to the activation of the $\nu_{N-H,sym}$ mode. Spectra (not shown) of ammonia adsorbed on support materials (CZ and CZP) are remarkable by very weak bands in intensity due to the weak acidity of ceria-based sample, in accordance with results previously obtained in NH_3 adsorption capacity measurements on stream (Table 4). Fig. S4 in the Supplementary Information file shows N—H bending modes of ammonia adsorbed on acidic sites. The bands at 1237 cm^{-1} and 1605 cm^{-1} are attributed to the symmetric and asymmetric deformation of NH_3 ($\delta(NH_3)$) coordinatively bound to Lewis acid sites, respectively [40]. Brønsted acid sites are highlighted by two bands at 1426 cm^{-1} and 1666 cm^{-1} assigned to $\delta_{as}(NH_4^+)$ and $\delta_s(NH_4^+)$, respectively. Acidic properties were enhanced by WO_3 or Nb_2O_5 deposits. Tungsten-containing catalysts showed the higher NH_3 adsorption together with higher Brønsted acid sites amount. Again, lower acid sites abilities are observed toward CZP formulation compared to CZ support.

3.5. Catalytic behaviors

The effect of partial substitution of Pr for Zr in CeZr-based supports in NH_3-SCR, NO and NH_3 oxidation experiments was first investigated for the supports alone (Fig. 5–1). The niobium loading on CZ or CZP support was thereafter examined. Results are reported in Fig. 5–2.

3.5.1. Catalytic behaviors of the supports; Praseodymium effect

First, the NH_3-SCR behavior of both supports, namely CZ (open symbol) and CZP (full symbol) was evaluated. Clearly, the deNO_x performances without W or Nb were not relevant since the ammonia consumption was not associated with NO_x reduction, except at 150 °C on CZP (Fig. 5A1). On the contrary, the outlet NO_x concentration increased, leading to negative NO_x conversions. On ceria-zirconia, no apparent NO_x reduction was recorded but the ammonia conversion was fully selective into N_2 until 350 °C (corresponding NH_3 conversion: 8 %). At higher temperatures, the ammonia conversion significantly increased and reached 70 % at 500 °C, but the selectivity into NO_x also increased with temperature, from 21 % at 400 °C to 82 % at 500 °C. NO_2 formation was also observed and the outlet NO_2/NO_x ratio was close to that observed during the NO oxidation test (Fig. 5B1): the NO oxidation into NO_2 occurred in a limited extent and the maximum NO conversion (23 %) was recorded at 400 °C. The NO oxidation activity decreased at high temperature ($T \geq 450$ °C) and tended to the thermodynamic equilibrium. Interestingly, the NH_3 conversion curve obtained in SCR condition was similar to that recorded without NO in the feed stream (NH_3 oxidation test (NH_3-SCO), Fig. 5C1). Again, the ammonia conversion led mainly to NO_x species, with higher selectivity compared to the SCR test, at 75 % and 90 % at 400 °C and 500 °C, respectively. Then, the CZ support was able to oxidize NO and NH_3, but the intermediate species did not allowed the NO_x reduction into N_2. Note that no N_2O was recorded during the catalytic tests. Finally, these catalytic behaviors clearly highlight the NH_3-NO_x and NH_3-O_2 competition reactions on the considered supports.

CZP support exhibited the same general behaviors as CZ: the SCR test showed mainly ammonia oxidation into NO_x species, and similar ammonia conversion curve was observed without NO in the feed stream. In addition, the NO oxidation activity was still moderate. However, the NH_3 conversion (with or without NO co-feeding) was significantly higher for CZP than CZ (Fig. 5A1 and C1, respectively), especially in the 250−450 °C temperature range. At 300 °C, the recorded ammonia conversion in the SCR test reached 35 % on CZP, and only 3%, on CZ. However, both supports exhibited NH_3 conversions close to 70 % at 500 °C. The selectivity in NH_3 oxidation into NO_x was also higher with CZP, at 80 % and 93 % at 400 °C and 500 °C, respectively. Finally, CZP exhibited higher oxidation behaviors compared to CZ.

3.5.2. Nb-supported catalysts

As expected, addition of niobium oxide on CZ support improved the NH_3 reactivity (NH_3-SCR, Fig. 5A2). The NO_x conversion curves classically exhibited a maximum near 400−450 °C. For higher temperatures, the NO_x conversion decreased, while the ammonia conversion still increased, indicating a competition between the NO_x reduction and the NH_3 oxidation. In fact, this competition was observed from approximately 300 °C with these samples since the standard or fast SCR stoichiometry reaction was respected only for lower temperatures. Fig. 5A2 (NO oxidation experiments) also shows that the partial substitution of Pr for Zr (Nb/CZP) led to a decrease in the NO_x conversion compared to Nb/CZ. The competition with the ammonia oxidation also appeared more noticeable on Nb/CZP since the gap between NO_x and NH_3 conversions was generally more marked. Measurements at 500 °C showed higher deactivation of the Nb/CZ sample compared to Nb/CZP, which is in accordance with a higher ammonia oxidation rate at this temperature

recorded during the ammonia oxidation test illustrated in Fig. 5C2 (NH_3-SCO experiments). The ammonia conversion at 500 °C was 51 % and 68 % for Nb/CZP and Nb/CZ, respectively. Moreover, compared to the bare supports, Nb addition on CZ improved the ammonia oxidation moderately, while Nb addition on CZP strongly inhibited it. Consequently, the ammonia conversion curves recorded with Nb containing catalysts were closer each other than for the corresponding supports. Note that the ammonia oxidation over Nb-containing catalysts was mainly selective in N_2. The maximum the NO_x selectivity was recorded at 500 °C and reached between 13 % and 17 % at 500 °C depending on the support (see the Supplementary Information file, Fig. S5). Concerning the NO oxidation behavior, the niobium addition led to an inhibition, whatever the considered support. For instance, the NO conversions at 400 °C were approximately half of those recorded with the supports, at only 9% and 11 % for Nb/CZ and Nb/CZP, respectively (Fig. 5B2).

3.5.3. W versus Nb supported catalysts

The NH_3-SCR behaviors of Nb and W-based catalysts supported on CZ or CZP are compared in Fig. 6. A complementary comparison of the NH_3-SCR behaviors of W-based catalysts supported on CZ or CZP is reported in Fig. S6 in the Supplementary Information (SI) file. Fig. 6A shows that the NO_x conversion recorded at 200 °C and 250 °C was lower for W/CZ than for Nb/CZ, but the opposite was observed from 350 °C to 550 °C. This behavior typically illustrates higher oxidation behavior on Nb/CZ compared to W/CZ, which promotes both (i) the low temperature deNO_x performances and (ii) the ammonia oxidation at high temperature, which competes with the NO_x reduction. This result is in accordance with the higher redox behavior of Nb/CZ compared to W/CZ (OSCC measurements and NO oxidation behavior (see below, Fig. 7A)). Even though W/CZ exhibited higher ammonia storage capacities than Nb/CZ, this parameter did not seem to be the driving force in this case. This results reveals that redox and acid behaviours intervene differently in the considered NO_x reduction by NH_3 and NH_3 oxidation reactional pathways, as developed in section 3.6.

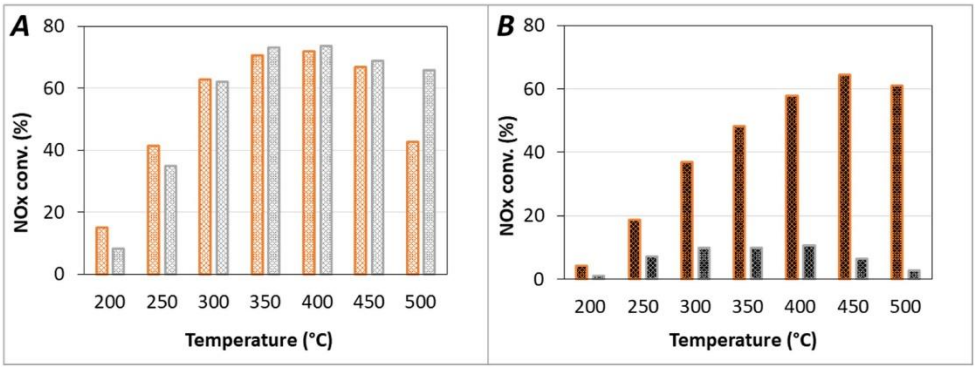

Fig. 6. NH_3-SCR behaviors : comparative effect in NO_x conversion of Nb (■) and W (■) catalysts supported on CZ (A) or CZP (B).

As previously described, Nb based catalyst was more efficient when niobium was supported on CZ compared to CZP (Fig. 5A1). This decrease in the deNO_x efficiency was more dramatically marked with W based catalysts. The W-CZP interaction was very detrimental for the NO_x reduction since the maximum NO_x conversion over W/CZP, recorded in the 300-400 °C temperature range, was close to 10 % (Fig. 6B). The corresponding ammonia conversion remained higher than the NO_x one, at 32 % at 300 °C and 68 % at 500 °C (Fig. S6 in SI file). However, these values were lower than on W/CZ (75 % and 93 %, respectively).

Compared to Nb-based catalysts, W-based samples showed poor NO oxidation behaviors (Fig. 7A), with maximum NO conversions of 4 % and 8 % (at 500 °C) for W/CZ and W/CZP, respectively. This detrimental effect of the W-CZP interaction on the NO oxidation rate was not observed for the ammonia oxidation behavior since W/CZP showed higher ammonia conversion than W/CZ in the 200−450 °C temperature range (Fig. 7B). However, while the W/CZ sample was very selective in N_2 (the maximum selectivity in NO_x reached only 5 % in the whole studied temperature range), the partial substitution of zirconium for praseodymium led to a significant increase in the NO_x selectivity, at 31–35 % in the 300−500 °C temperature range for W/CZP sample (Fig. S5). This result confirms that the W/CZP catalyst was still active in ammonia activation, but it mainly promoted the NH_3 oxidation instead of the NO_x reduction (Fig. S6 in SI file). Consequently, the gap between the NO_x conversion and the NH_3 conversion during the SCR test was significantly higher on W/CZP than for other studied catalysts. The characterizations of this catalyst showed that W/CZP exhibited both the poorer redox behavior and the lower acidity (acid sites strength and number).

To conclude, it clearly appears that NO_x SCR performances are strongly affected by the catalyst formulation, together with the surface and bulk properties. The next part is devoted to the relationship between the chemical properties of the materials and the catalytic results in order to detail the key steps in the $deNO_x$ mechanism on acidic oxides.

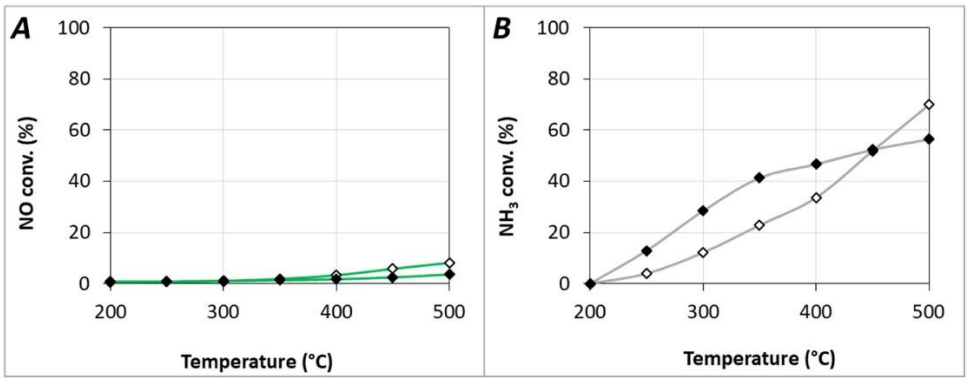

Fig. 7. Catalytic performances of W-supported catalysts (W/CZ: ◇, open symbol); W/CZP: ◆, full symbol) in A: NO oxidation (—); B: NH_3 oxidation (—).

3.6. Key parameters in $deNO_x$ chemistry

As previously mentioned, NH_3-SCR mechanism is complex and addresses a bi-functional active sites catalysis (redox and acid), together with a surface reaction respecting mainly the Eley-Rideal type depending on reactive compounds. To gain insight on the influence of both the praseodymium incorporation in the support formulation and the acidic properties induced by W or Nb loading, tentative multi-site correlations were undertaken in 3-dimensional (3D) graphics (Fig. 8, Fig. 9). The main conclusions are also illustrated by usual 2 dimensions (2D) correlations in the Supplementary Information file (Figs. S7–S9).

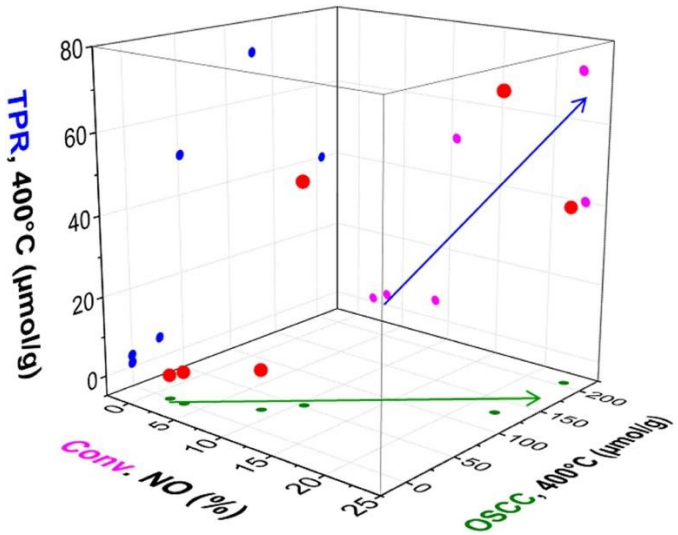

Fig. 8. Red points denote the 3D relationship between the NO oxidation experiments and the NO conversion into NO_2 (%) at 400 °C (X), the OSCC ($\mu mol_O\ g^{-1}$) measured at 400 °C (Y) and the H_2 consumption ($\mu mol_{H2}\ g^{-1}$) recorded in the 20-400 temperature range during the H_2-TPR test (Z). XY projection in green, ZX projection in pink, YZ projection in blue.

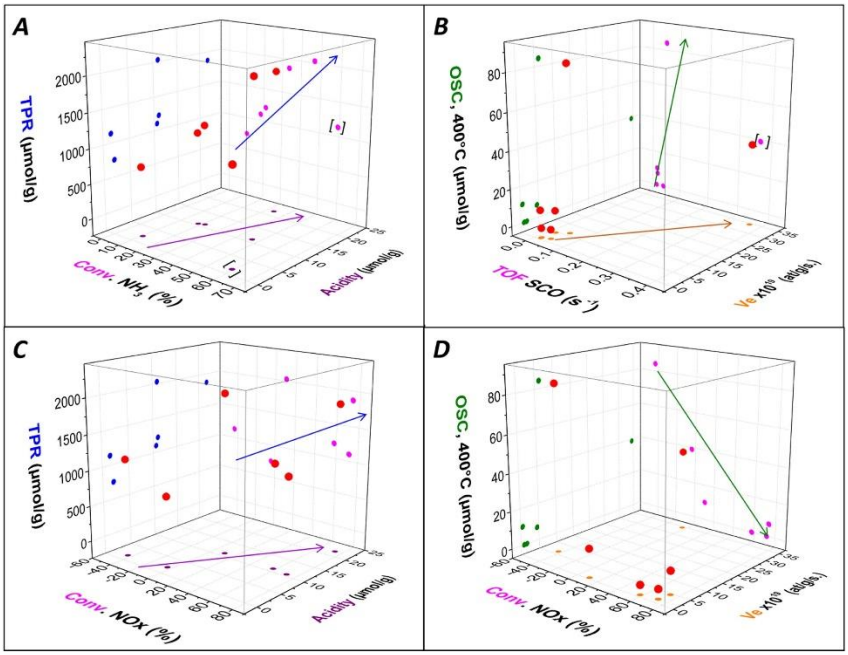

Fig. 9. Red points denote the 3D relationship for NH_3-SCO (A, B) or NH_3-SCR (C,D) between: (A, C): NH_3 conversion (A, %) or NO_x conversion (C, %) at 400 °C (X), Acidity ($\mu mol_{NH3}/g$) determined at 200 °C (Y), H_2-TPR consumption recorded in the 20–1000 °C temperature range ($\mu mol_{H2}\ g^{-1}$) (Z). XY projection in purple, ZX projection in pink, YZ projection in blue; (B, D): TOF in NH_3 conversion (s^{-1}) at 400 °C (B) calculated as NH_3 converted (mol $g^{-1}\ s^{-1}$) by active sites (mol g^{-1}) or NO_x conversion (D, %) at 400 °C (X), initial $^{18}O_2$ exchange rate (Ve, at $g^{-1}\ s^{-1}$) (Y), OSC measurements ($\mu mol_O\ g^{-1}$) at 400 °C (Z). XY projection in orange, ZX projection in pink, YZ projection in green.

The redox and oxygen mobility properties of the samples, key parameters driving the $deNO_x$ performances, were investigated by complementary techniques in addition to usual H_2-TPR analysis, namely the OSC/OSCC measurement by CO, and the isotopic exchange of oxygen. Additionally, NO and NH_3 oxidation experiments performed under a continuous reaction flow were also considered to get information about the oxidation pathways involved in the NH_3-SCR reaction.

Finally, the acidity, another limiting step in the SCR activity, was estimated by ammonia storage measurements at different temperatures using a gas flow containing CO_2 and H_2O (Table 1). This technique enables quantitative analysis and evaluation of the thermal stability of adsorbed species.

3.6.1. Insight into NO oxidation

As shown in section 3.2.2, niobium and tungsten addition significantly decreased the complete oxygen storage capacity of CZ and CZP support. This effect was especially pronounced for supported tungsten samples, with nearly no OSCC at 400 °C for W/CZ and W/CZP. These results are in good agreement with H_2-TPR profiles recorded up to 400 °C (section 3.2.1) and illustrate stronger surface interaction of W with CZ or CZP compared to Nb-containing catalysts.

Fig. 8 reports in 3-dimensional (3D) graphic these characterization depending on the NO oxidation behavior at 400 °C. The XY projection reported in green in Fig. 8 clearly indicates that NO oxidation rates are correlated to OSCC results. Higher the NO conversion, higher the OSCC amount. It induces that NO oxidation mechanism follows similar pathway than CO oxidation with lattice oxygen atoms. A less evident correlation with the H_2 consumption recorded up to 400 °C (from H_2-TPR experiments) is denoted, as depicted by the ZX projection in pink. It tends to indicate that NO oxidation is mainly driven by the availability of reactive oxygen species from the support and undergoes *via* a Mars and van Krevelen type reaction, according to reaction (4) [41]:

$$NO + O_{(s)} \rightarrow NO_2 \qquad (4)$$

3.6.2. Insight into NH_3 oxidation

As previously exposed in the introduction part, it is assumed that ammonia reactivity requires prior chemisorption on acidic sites. Subsequently, NH_3-ad species undergo hydrogen abstraction. It induces thereafter the participation of oxygen species for the regeneration of active sites due to the reduction of catalyst by H-ad compound. Consequently, to go further in NH_3 oxidation mechanism (NH_3-SCO), chemical characterization of catalysts, namely H_2-TPR, acidity, OSC and isotopic exchange experiments, have been plotted in 3 dimensions (3D) correlation in regards on catalytic performances in ammonia oxidation recorded at 400 °C (Fig. 9A, B). Acidic properties were evaluated by NH_3 capacity measurements at 200 °C to avoid the reducer consumption by CZ and CZP samples at higher temperature (Fig. 4A, Table 4). In this section the participation of O_2 in NH_3 oxidation and reoxidized active site is tentatively discussed.

Overall, the three parameters in Fig. 9A are related and the red marks (X,Y,Z coordinates) increase continuously with acidity and TPR results. Nevertheless, it is important to note that acidity is not a limiting step for NH_3 oxidation since CZP support presented the higher ammonia oxidation rate together with a low acid sites amount (symbol in brackets on Fig. 9A). A clear trend emerges from the projected conversion of NH_3 to acidic properties (XY projection reported in violet, Fig. 9A), apart from the CZP sample shown in square brackets as already discussed. In addition, higher the NH_3 oxidation rate, higher the total H_2 consumption evaluated from TPR experiments (ZX projection in pink). Consequently, ammonia activation is evidenced by bifunctional catalysis with the two-component acidity and redox properties or oxygen availability. It results that the first step in NH_3 oxidation pathway is assumed to be the adsorption of ammonia on acid sites (Eq. 5, where * represents active sites) by electron donation of ammonia to Lewis acid sites for instance. It is postulated that the hydrogen abstraction follows the NH_3 adsorption, as already proposed by Rezaei et al. [42]. Note that the disproportionation reaction of coordinated NH_3 according to $2NH_3 \leftrightarrows NH_4 + NH_2$ is less likely, as reported by Kijlstra et al. [43].

The partial ammonia oxidation releases a hydrogen atom (Eq. 6), which is assumed to be involved in the reduction of the support (illustrated by Eq. 7 with cerium, but Pr^{IV} species can also be considered) and support the ZX projection correlation in pink on Fig. 9A. The sum of Eqs. (5), (6), (7) results in global Eq. 8. This part also highlights the Lewis to Brønsted acid sites transformation mentioned in the introduction part [11].

$$2NH_3 + 2^* \rightarrow 2NH_3^* \quad (5)$$

$$2NH_3^* + 2^* \rightarrow 2NH_2^* + 2H^* \quad (6)$$

$$2Ce^{IV} + 2H^* \rightarrow 2Ce^{III} + 2H^{+}* \quad (7)$$

$$2NH_3 + 2Ce^{IV} + 4^* \rightarrow 2NH_2^* + 2Ce^{III} + 2H^{+}* \quad (8)$$

As a result, in order to determine an activity per site and to illustrate the role of oxygen in the NH_3 oxidation mechanism, the ammonia oxidation rate (mol g^{-1} s^{-1}) at 400 °C was expressed as a turnover frequency (TOF, s^{-1}), taking into account the amount of acidic sites determined at 200 °C. Globally, results are correlated and the red plots in Fig. 9B regularly increases with OSC and initial exchange rate measurements. In addition, except for the CZP sample (shown in the Fig. 9 in square brackets), some interesting trends are obtained. Thus, it appears that the NH_3 oxidation activity per site increases with the OSC values as shown in the pink ZX projection, and then suggests the involvement of dynamic surface O^{2-} ions. A less clear trend is obtained with the initial exchange rate, although it would seem that this parameter is also involved (XY projection in orange). Overall, these results highlight a complex bifunctional mechanism for NH_3 oxidation where adsorption and H abstraction have to be postulated to support results from Fig. 9A,B (Eq. (5), (6). Overall, hydrogen abstraction results in the reduction of catalyst and ammonia oxidation rate requires surface oxygen mobility to regenerate both active sites (Eq. 9) and NH_x ad-species (Eq. 10). Thus, the role of gaseous O_2 is postulated to regenerate the catalyst surface and to complete the catalytic cycle loop reaction as reported by Zhao et al. [44]. Note that the sum of Eqs. (8), (9), (10) results in the NH_3-SCO stoichiometry (Eq. 11).

$$2Ce^{III} + \tfrac{1}{2}O_2 \rightarrow 2Ce^{IV} + O^{2-} \quad (9)$$

$$2NH_2^* + O_2 \rightarrow N_2 + 2H_2O + 2^* \quad (10)$$

$$2NH_3 + 3/2\ O_2 \rightarrow N_2 + 3H_2O \quad (11)$$

3.6.3. Insight into NH_3-SCR

Similar 3D correlations are reported in Fig. 9C and D for NO_x conversion obtained at 400 °C in NH_3-SCR experiments depending on same chemical behaviors than previously discussed, namely H_2-TPR, acidity, OSC and isotopic exchange experiments.

The global pattern reported in Fig. 9C shows that deNO_x performances increase as a whole with both acidic properties and total reducibility (H_2-TPR) of catalysts. Interestingly, the correlation is more obvious with the acidic properties, as illustrated by the XY projection (reported in purple). As mentioned for the NH_3-SCO experiments, it highlights the involvement of ammonia adsorption as the first step of NH_3-SCR mechanism, together with NH_3-SCO scheme (Eq. 8).

Controversially, opposite relationship is observed regarding oxygen activation (availability/exchange), as denoted in Fig. 9D. The ZX projection (reported in pink) clearly illustrates that higher the NO_x conversion, lower the OSC measurements. With the assumption of active site regeneration by O_2 availability (Eq. 9), it induces a strong competition with the SCR reactivity. It is assumed that a new favored reaction occurs in the presence of NO with NH_2-ad species oxidation (Eq. 12). Note that the sum of reactions (8), (9) and (12) give rise to the global standard SCR stoichiometry (Eq. 1).

$$2NH_2^* + 2NO \rightarrow 2NH_2NO^* \rightarrow 2N_2 + 2H_2O + 2^* \qquad (12)$$

It also induces that the NH_3-SCR (Eq. 1) reaction is competitive with NH_3-SCO (Eq. 11) through the common activated NH_2 amide species, as already proposed in [45]. As reported in many works, the global Eq. 12 reaction involves nitrosamine (NH_2NO) intermediate as highly reactive compound for NO_x reduction [46,47]. Finally, based on the works of Ramis et al. [45,48], the reported data allow to confirm the reaction Scheme 1 to illustrate O_2/NO competitive reactivity in regard to NH_3 ad-species. The oxidative dehydrogenation of NH_3 to active NH_2 species is decisive for SCR performances because NH_2 amide species could directly react with gaseous NO by an appropriate Eley-Rideal mechanism to generate NH_2NO intermediates that are subsequently decomposed to N_2 and H_2O [49]. To evidence that the NH_3-SCR reaction follows an Eley-Rideal mechanism, a DRIFT study was performed on W/CZ sample. This catalyst was selected because it showed the higher NH_3 adsorption behavior (Table 4 and Fig. S4). Results reported in section 7 of the SI file indicates that Lewis acid sites are involved at low temperature in the NO_x reduction by NH_3. Spectral feature of nitrates or water adsorbed species as reaction product of NO_x reduction were observed from RT. At higher temperature (150 °C), ammonia species adsorbed on Brønsted acid sites were consumed under NO flow. These experiments highlighted that gaseous NO can react with adsorbed NH_3 compounds, following an Eley-Rideal mechanism.

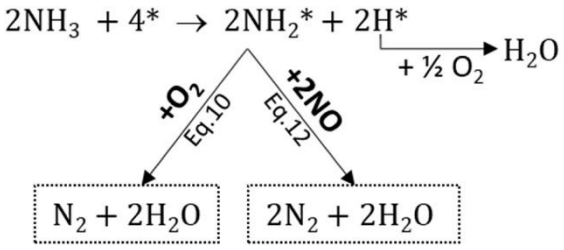

Scheme 1. Proposed reaction scheme for NH^3 oxidation by O_2 or NO.

The main correlation trends and mechanistic conclusions are also evidenced with usual 2 dimensions (2D) correlation in the Supplementary Information file (Figs. S7–S9).

Consequently, lower deNO_x performances were achieved with W/CZP sample which presents high ammonia oxidation activity by oxygen (Fig. 7B), with significant NO_x formation (Fig. S5). With this catalyst, the competition between SCR and ammonia oxidation illustrated in Scheme 1 was also evidenced in Fig. S6, especially for temperatures higher than 400 °C. It is proposed that W^{6+} (χ = 1.7, Electronegativity Pauling scale) create stronger covalent bond with oxygen than Nb^{5+}(χ = 1.8, Electronegativity Pauling scale) taking into account the electronegativity, the ionic radii in [6]-fold coordination (r(Nb^{5+}) =0.64 Å and r(W^{6+}) =0.58 Å) and the valence state Z relating to the polarizing character Z2/r of the dopants (W, Nb). Thus, it outlines the larger Lewis acid character of W associated to the higher polarizing character

and electronegativity. It is interesting to mention that χ (Ce) = 1.1 = χ (Pr), whereas χ (Zr) remains higher at χ (Zr) = 1.4. Thus, the ability of W^{6+} to be associated to Pr^{3+} basic sites *via* oxygen bonding is strongly improved, then explaining the Pr^{3+}-O-W^{6+} interactions which prevent the $deNO_x$ activity, poisoned by the dual Lewis acid and basic centers. Compared with CZP-based catalysts, supported CZ catalysts (W/CZ and Nb/CZ) presented higher NO_x conversion (with lower W^{6+}/Nb^{5+}-O-Ce^{4+} interactions than W^{6+}/Nb^{5+}-O-Pr^{3+}), together with moderate SCO performance (Fig. 5C2, Fig. 7B). These results suggest the beneficial formation of NH_2NO intermediate for high SCR performances, impacted by tuning the valence of elements and acid-base properties of catalysts. Note that additional analyses of the electronic structure of CZP and Nb/CZP samples were performed by X-Ray photoelectron spectroscopy (XPS). Results are reported in the Supplementary Information file (Figs. S13 and S14) and highlight the effective interactions of acid oxide with Ce^{4+} and Pr^{3+}.

Accordingly, the resulting surface NH_2* species has to react with weakly adsorbed or gaseous NO to form the surface NH_2NO* intermediate complex that spontaneously decomposes to N_2 and H_2O (Eq. 12). As a consequence, Nb and W loading is suspected to turn the electronic interaction between the metal and the CZ/CZP support and impacted the oxygen vacancies and active oxygen. Therefore, it contributes to the high activity of W/CZ and Nb/CZ catalysts by subsequent reaction of NH_2-ad species and NO, as a crucial step for the NH_2NO formation [50]. In addition, note that the decomposition of NH_2NO was evidenced to occur on Brønsted acid sites [51]. Then, in accordance with Fig. S4 (IR spectra of adsorbed ammonia monitored by FTIR), higher Brønsted acid sites amount of W/CZ and Nb/CZ catalysts is consistent with high SCR activity. Finally, SCR $deNO_x$ activity is not correlated to NO oxidation behavior, since W/CZ sample presents both higher $deNO_x$ performances together with lower NO oxidation properties (Fig. 7A), confirming that surface NO adsorption (Eq. 4) is not part of SCR mechanism, supporting an Eley-Rideal-type reaction.

4. Conclusion

The main aim of this study was to propose an overview of NH_3-NOx and NH_3-O_2 competitive reactions depending on redox and acid behaviors, based on the modification by praseodymium of a ceria-zirconia support for tungsten and niobium supported catalysts. The partial substitution of zirconium for praseodymium (CZP) favored the support reducibility by H_2 with both a decrease in the starting reduction temperature and an increase of the total amount of reducible species. The oxygen exchange process, evaluated by isotopic exchange, was also improved since the initial exchange rate was five times higher over CZP compared to CZ material. On the contrary, the amount of reactive oxygen toward CO was lower over CZP sample than on CZ (OSC-OSCC measurements). It highlights that reducibility of CZ/CZP materials is strongly dependent on the reductant agent, with different reduction mechanisms between CO and H_2 induced by praseodymium insertion. However, the three characterization techniques (H_2-TPR, OSC-OSCC and IE) showed that both Nb_2O_5 and WO_3 impregnation strongly inhibited the redox behaviours. The more marked effect was clearly observed with WO_3 deposited on CZP. At the same time, niobium and tungsten oxides addition also provided acidic sites for NH_3 adsorption, an elementary step in NH_3-SCR mechanism. On CZ, WO_3 addition led to double NH_3 storage capacities compared to Nb_2O_5, but praseodymium in CZ inhibited the ammonia adsorption on Nb-containing sample and in a higher extent on W-based catalysts. As expected, the surface properties alteration strongly affected the NO_x SCR performances which in turn became dependent on the catalyst formulation. Nb_2O_5 or WO_3-based catalyst were more efficient when the acidic oxide was supported on CZ compared to CZP. Especially, the W-CZP interaction was very detrimental for the NO_x reduction.

The NO oxidation rates were correlated to OSC-OSCC results, indicating that the NO oxidation mechanism follows similar pathway than CO oxidation, involving lattice oxygen by a Mars and Van Krevelen type mechanism. NO oxidation is reported to not be the driving force in the NO_x reduction reaction. 3D correlations indicated that ammonia oxidation respects a bifunctional catalysis with the two-component acidity and oxygen availability, the involvement of surface O^{2-} ions being suggested. As expected, the $deNO_x$ performances increase as a whole with both acidic and total reducibility (H_2-TPR) of catalysts, but the trend was more marked with the acidic properties. In fact, lower is the OSC measurement, higher is the NO_x conversion, which reflected a strong competition between the NO_x SCR from the formation of highly reactive nitrosamine (NH_2NO) intermediates and the ammonia oxidation. A reaction scheme for NH_3 oxidation by O_2 or NO is proposed which tentatively illustrates that the reaction mechanism begins by the oxidative dehydrogenation of NH_3 (on acid sites). The generated species then react either with oxygen species (mainly from the catalyst) or with gaseous NO by an Eley-Rideal mechanism.

CRediT authorship contribution statement :

- **Charlotte Croisé:** Investigation (catalytic tests and characterizations).
- **Rémy Pointecouteau:** Investigation (catalysts preparation and characterizations).
- **Joudia Akil:** Investigation (catalytic tests and characterizations), review & editing.
- **Alain Demourgues:** Resources, methodology, funding acquisition, formal analysis (XRD), review & editing.
- **Nicolas Bion:** Resources, methodology, funding acquisition, formal analysis (isotopic exchange).
- **Xavier Courtois:** conceptualization, methodology, resources, writing original draft, review & editing, formal analysis (catalytic tests, H2 TPR, NH3 adsorption).
- **Fabien Can:** conceptualization, methodology, resources, visualization, writing original draft, review & editing, formal analysis (catalytic tests, FTIR).

Declaration of Competing Interest : The authors report no declarations of interest.

Acknowledgements : The authors gratefully acknowledge the French National Agency for Research (ANR, Coral Project, ref. ANR-17-CE08-0022-03), the Regional Council of Nouvelle Aquitaine, the French Ministry of Research and the European Regional Development Fund (ERDF) for financial supports.

Appendix A. Supplementary data : The following is Supplementary data to this article: Download : Download Acrobat PDF file (1MB)

References

1. J.P. Chen, R.T. Yang. **Role of WO_3 in mixed V_2O_5-WO_3/TiO_2 catalysts for selective catalytic reduction of nitric oxide with ammonia.** Appl. Catal. A, 80 (1992), pp. 135-148.
2. M. Seneque, F. Can, D. Duprez, X. Courtois. **NO_x selective catalytic reduction (NO_x-SCR) by urea: evidence of the reactivity of HNCO, including a specific reaction pathway for NO_x reduction involving NO + NO_2.** ACS Catal., 6 (7) (2013), pp. 4064-4067.
3. M. Seneque, X. Courtois, F. Can, D. Duprez. **Direct comparison of urea-SCR and NH_3-SCR activities over acidic oxide and exchanged zeolite prototype powdered catalysts.** Top. Catal., 59 (2016), pp. 938-944.
4. X. Liu, X. Wu, T. Xu, D. Weng, Z. Si, R. Ran Chin. **Effects of silica additive on the NH_3-SCR activity and thermal stability of a V_2O_5/WO_3-TiO_2 catalyst.** J. Catal., 37 (2016), pp. 1340-1346.
5. S. Brandenberger, O. Kröcher, A. Tissler, R. Althoff. **The state of the art in selective catalytic reduction of NO_x by ammonia using metal-exchanged zeolite catalysts.** Catal. Rev., 50 (2008), pp. 492-531.
6. N. Apostolescu, B. Geiger, K. Hizbullah, M.T. Jan, S. Kureti, D. Reichert, F. Schott, W. Weisweiler. **Selective catalytic reduction of nitrogen oxides by ammonia on iron oxide catalysts.** Appl. Catal. B, 62 (2006), pp. 104-114.
7. G.S. Qi, R.T. Yang, R. Chang. **MnO_x-CeO2 mixed oxides prepared by co-precipitation for selective catalytic reduction of NO with NH_3 at low temperatures.** Appl. Catal. B, 51 (2004), pp. 93-106.
8. Z. Lian, F. Liu, H. He, X. Shi, J. Mo, Z. Wu. **Manganese–niobium mixed oxide catalyst for the selective catalytic reduction of NO_x with NH_3 at low temperatures.** Chem. Eng. J., 250 (2014), pp. 390-398.
9. S. Verdier, E. Rohart, H. Bradshaw, D. Harris. **Acidic Zirconia Mixed Oxides Are Described As Attractive Alternatives for the NH3-SCR Application. SAE Technical Paper 2008-01-1022.** (2008), 10.4271/2008-01-1022
10. L. Bisson, J. Hernandez, R.M.J.C. Marques, E. Rohart, M. Bortun, D.J. Harris, C. Jones, Method for treating a gas containing nitrogen oxides (NOx), using a composition comprising zirconium, cerium and niobium as a catalyst, world patent WO2013037507A1 (2013).
11. H. Liu, C. You, H. Wang. **Time-resolved in-situ IR and DFT study: NH_3 adsorption and redox cycle of acid site on vanadium-based catalysts for NO abatement via selective catalytic reduction.** Chem. Eng. J., 382 (2020), pp. 122756-122764.

12. Y. Peng, K. Li, J. Li. **Identification of the active sites on CeO_2-WO_3 catalyst for SCR of NO_x with NH_3: an in situ IR and Raman spectroscopy study.** Appl. Catal. B, 140-141 (2013), pp. 483-492.
13. W.D. Wang, P.Y. Lin, Y.L. Fu, C.Y. Cao. **Redox properties and catalytic behavior of praseodymium-modified (Ce-Zr)O_2 solid solutions in three-way catalysts.** Catal. Lett., 82 (2002), pp. 19-27.
14. J. Abel, M. Lamirand-Majimel, J. Majimel, V. Bellières-Baca, V. Harlé, G. André, C. Prestipino, S. Figueroa, E. Durand, A. Demourgues. **Oxygen non-stoichiometry in $Pr_{1-x}Zr_xO_{2-y}$ compounds (0.02<x<0.5).** Dalton Trans., 43 (2014), pp. 15183-15191.
15. H.W. Jen, G.W. Graham, W. Chun, R.W. McCabe, J.P. Cuif, S.E. Deutsch, O. Touret. **Characterization of model automotive exhaust catalysts: Pd on ceria and ceria–zirconia supports.** Catal. Today, 50 (1999), pp. 309-328
16. V. Frizon, J.M. Bassat, M. Pollet, E. Durand, J. Hernandez, K. Pajot, P. Vernoux, A. Demourgues. **Tuning the Pr valence state to design high oxygen mobility, redox and transport properties in the CeO_2-ZrO_2-PrO_x phase diagram.** J. Phys. Chem. C, 123 (2019), pp. 6351-6362.
17. Y. Li, H. Cheng, D. Li, Y. Qin, Y. Xie, S. Wang. **WO_3/CeO_2-ZrO_2, a promising catalyst for selective catalytic reduction (SCR) of NO_x with NH_3 in diesel exhaust.** Chem. Commun. (2008), pp. 1470-1472.
18. F. Can, S. Berland, S. Royer, X. Courtois, D. Duprez. **Composition-dependent performance of $Ce_xZr_{1-x}O_2$ mixed-oxide-supported WO_3 catalysts for the NO_x storage reduction–selective catalytic reduction coupled process.** ACS Catal., 3 (2013), pp. 1120-1132.
19. Y. Jiang, Z. Xing, X. Wang, S. Huang, X. Wang, Q. Liu. **Activity and characterization of a Ce–W–Ti oxide catalyst prepared by a single step sol–gel method for selective catalytic reduction of NO with NH_3.** Fuel, 151 (2015), pp. 124-129.
20. L. Chen, D. Weng, Z. Si, X. Wu. Prog. Nat. Sci.-Mater. Int., 22 (2012), pp. 265-272.
21. W. Shan, F. Liu, H. He, X. Shi, C. Zhang. **Novel cerium–tungsten mixed oxide catalyst for the selective catalytic reduction of NO_x with NH_3.** Chem. Commun., 47 (2011), pp. 8046-8048.
22. R. Qu, X. Gao, K. Cen, J. Li. **Relationship between structure and performance of a novel cerium-niobium binary oxide catalyst for selective catalytic reduction of NO with NH3.** Appl. Catal. B: Environ., 142–143 (2013), pp. 290-297.
23. Z. Ma, D. Weng, X. Wu, Z. Si, B. Wang. **A novel Nb–Ce/WOx–TiO2 catalyst with high NH3-SCR activity and stability.** Catal. Commun., 27 (2012), pp. 97-100.
24. Z. Ma, X. Wu, Z. S, D. Weng, J. Ma, T. Xu. **Impacts of niobia loading on active sites and surface acidity in NbOx/CeO2-ZrO2 NH3-SCR catalysts.** Appl. Catal. B, 179 (2015), pp. 380-394
25. Z. Lian, F. Liu, H. He, K. Liu. **Nb-doped VO_x/CeO_2 catalyst for NH_3-SCR of NO_x at low temperatures.** RSC Adv., 5 (2015), pp. 37675-37681.
26. P. Maitarad, J. Meeprasert, L. Shi, J. Limtrakul, D. Zhang, S. Namuangruk. **Mechanistic insight into the selective catalytic reduction of NO by NH_3 over low-valent titanium-porphyrin: a DFT study.** Catal. Sci. Technol., 6 (11) (2016), pp. 3878-3885.
27. S. Ding, F. Liu, X. Shi, H. He. **Promotional effect of Nb additive on the activity and hydrothermal stability for the selective catalytic reduction of NO_x with NH_3 over $CeZrO_x$ catalyst.** Appl. Catal. B, 180 (2016), pp. 766-774.
28. M.S. Soares, R.D. Barbosa, G.M. da Cruz, J.A.J. Rodrigues, S. Ribeiro. **Effect of niobium addition in support catalysts applied in satellite propulsion.** Mater. Chem. Phys., 189 (2017), pp. 153-161.
29. J.A. Sommers. **Hydrolysis of Niobium Pentachloride Solutions, the Metallurgical Society (TMS) Annual Meeting and Exhibition.** San Diego (1992)
30. S. Kacimi, J. Barbier Jr., R. Taha, D. Duprez. **Oxygen storage capacity of promoted Rh/CeO_2 catalysts. Exceptional behavior of RhCu/CeO_2.** Catal. Lett., 22 (1993), pp. 343-350.
31. N.K. Gamboa-Rosales, J.L. Ayastuy, Z. Boukha, N. Bion, D. Duprez, J.A. Pérez-Omil, E. del Río, M.A. Gutiérrez-Ortiz. **Ceria-supported Au–CuO and Au–Co_3O_4 catalysts for CO oxidation: an $^{18}O/^{16}O$ isotopic exchange study.** Appl. Catal. B, 168-169 (2015), pp. 87-97.
32. Y. Madier, C. Descorme, A.M. Le Govic, D. Duprez. **Oxygen mobility in CeO_2 and $Ce_xZr_{(1-x)}O_2$ compounds: study by CO transient oxidation and $^{18}O/^{16}O$ isotopic exchange.** J. Phys. Chem. B, 103 (1999), pp. 10999-11006.
33. Y. Liu, C. Wen, Y. Guo, X. Liu, J. Ren, G. Lu, Y. Wang. **Mechanism of CO disproportionation on reduced Ceria.** ChemCatChem, 2 (2010), pp. 336-341.

34. D. Martin, D. Duprez. **Mobility of surface species on oxides. 1. Isotopic exchange of $^{18}O_2$ with ^{16}O of SiO_2, Al_2O_3, ZrO_2, MgO, CeO_2, and CeO_2-Al_2O_3. Activation by noble metals. correlation with oxide basicity.** J. Phys. Chem., 100 (1996), pp. 9429-9438.
35. M. Ziolek. **Niobium-containing catalysts—the state of the art.** Catal. Today, 78 (2003), pp. 47-64.
36. Z. Ma, X. Wu, Y. Feng, Z. Si, D. Weng, L. Shi. **Low-temperature SCR activity and SO_2 deactivation mechanism of Ce-modified V_2O_5–WO_3/TiO_2 catalyst.** Prog. Nat. Sci., 25 (2015), pp. 342-352.
37. I. Tankov, B. Pawelec, K. Arishtirova, S. Damyanova. **Structure and surface properties of praseodymium modified alumina.** Appl. Surf. Sci., 258 (2011), pp. 278-284.
38. J. Giménez-Mañogil, N. Guillén-Hurtado, S. Fernández-García, X. Chen, J.J. Calvino-Gámez, A. García-García. **Ceria-praseodymia mixed oxides: relationships between redox properties and catalytic activities towards NO oxidation to NO_2 and CO-PROX reactions.** Top. Catal., 59 (2016) 14095-10700.
39. D. Duprez, C. Descorme, T. Birchem, E. Rohart. **Oxygen storage and mobility on model three-way catalysts.** Top. Catal., 16/17 (2001), pp. 49-56.
40. W. Tan, J. Wang, L. Li, A. Liu, G. Song, K. Guo, Y. Luo, F. Liu, F. Gao, L. Dong. **Gas phase sulfation of ceria-zirconia solid solutions for generating highly efficient and SO_2 resistant NH_3-SCR catalysts for NO removal.** J. Hazard. Mater., 388 (2020), Article 121729.
41. D. Widmann, R.J. Behm. **Activation of molecular oxygen and the nature of the active oxygen species for CO oxidation on oxide supported Au catalysts.** Acc. Chem. Res., 47 (3) (2014), pp. 740-749.
42. E. Rezaei, B. Schlageter, M. Nemati, B. Predicala. **Evaluation of metal oxide nanoparticles for adsorption of gas phase ammonia.** J. Environ. Chem. Eng., 5 (2017), pp. 422-431.
43. W.S. Kijlstra, D.S. Brands, E.K. Poels, A. Bliek. **Mechanism of the selective catalytic reduction of NO by NH_3 over MnO_x/Al_2O_3.** J. Catal., 171 (1997), pp. 208-218
44. Q. Zhao, B. Chen, J. Li, X. Wang, M. Crocker, C. Shi. **Insights into the structure-activity relationships of highly efficient CoMn oxides for the low temperature NH_3-SCR of NO_x**. Appl. Catal. B, 277 (2020), Article 119215.
45. G. Ramis, L. Yi, G. Busca, M. Turco, E. Kotur, R.J. Willey. **Adsorption, activation and oxidation of ammonia over SCR catalysts.** J. Catal., 157 (1995), pp. 523-535.
46. J. Li, H. Chang, L. Ma, J. Hao, R.T. Yang. **Low-temperature selective catalytic reduction of NO_x with NH_3 over metal oxide and zeolite catalysts—a review.** Catal. Today, 175 (2011), pp. 147-456.
47. F. Gao, X. Tang, H. Yi, S. Zhao, C. Li, J. Li, Y. Shi, X. Meng. **A review on selective catalytic reduction of NO_x by NH_3over Mn–based catalysts at low temperatures: catalysts, mechanisms, kinetics and DFT calculations.** Catalysts, 7 (2017), p. 199.
48. G. Ramis, L. Yi, G. Busca. **Ammonia activation over catalysts for the selective catalytic reduction of NO, and the selective catalytic oxidation of NH_3. An FT-IR study.** Catal. Today, 28 (1996), pp. 373-380.
49. L. Han, S. Cai, M. Gao, J. Hasegawa, P. Wang, J. Zhang, L. Shi, D. Zhang. **Selective catalytic reduction of NO_x with NH_3 by using novel catalysts: state of the art and future prospects.** Chem. Rev., 119 (2019), pp. 10916-10976.
50. Z. Ma, X. Wu, Z. Si, D. Weng, J. Ma, T. Xu. **Impacts of niobia loading on active sites and surface acidity in NbO_x/CeO_2–ZrO_2 NH_3–SCR catalysts.** Appl. Catal. B, 179 (2015), pp. 380-394.
51. S. Soyer, A. Uzun, S. Senkan, I. Onal. **A quantum chemical study of nitric oxide reduction by ammonia (SCR reaction) on V_2O_5 catalyst surface.** Catal. Today, 118 (2006), pp. 268-278.